Journal of Cardiothoracic Surgery

RESEARCH Open Access

Application feasibility of virtual models and computational fluid dynamics for the planning and evaluation of aortic repair surgery for Williams syndrome

Jixiang Liang[1,4], Xuewei Fang[1*], Dianyuan Li[2], Guangyu Pan[3], Gen Zhang[2] and Bingheng Lu[1]

Abstract

Background Accurate diagnosis and evaluation of Williams Syndrome (WS) are essential yet challenging for effective surgical management. This study aimed to quantify the hemodynamic changes of surgical repair for WS through virtual surgery and computational fluid dynamics (CFD) for surgical guidance and postoperative evaluation.

Methods A patient preliminarily diagnosed with WS was included in this study. 3D model alongside hemodynamic analysis was used to guide and evaluate the surgical procedure. Preoperative, predictive and postoperative models were created and analyzed using CFD. Key parameters, including blood flow velocity, pressure differences, wall shear stress, and other critical factors, were assessed to evaluate the surgery's effectiveness.

Results In the hemodynamics analysis, the CFD results of predictive model and postoperative model demonstrated a high level of consistency, and showed significant differences compared to the preoperative model. The velocity at the stenosis on the aorta decreased from 5.6 m/s before the operation to 1.6 m/s in the virtual model and 1.5 m/s in the postoperative model. Surgical repair increased the proportion of outlet flow of the descending aorta (dAo) from 28.7% to 35.5%.

Conclusions Virtual surgery and CFD can predict surgical outcomes, enabling doctors to optimize and rehearse the procedure before the actual surgery. The method of predicting surgery through virtual surgery and CFD is accurate and feasible.

Trial registration Registered by the Ethics Committee of Peking University International Hospital (No. IRB2019-062).

Keywords Williams syndrome, Aortic repair, Virtual models, Computational fluid dynamics, Surgical planning

*Correspondence:
Xuewei Fang
xueweifang@mail.xjtu.edu.cn
[1]School of Mechanical Engineering, Xi'an Jiaotong University, No. 99 Yan Cheung Road, Shaanxi, Shaanxi, China
[2]Department of Cardiovascular Surgery, Nanjing Medical University Affiliated Suzhou Hospital: Suzhou Municipal Hospital, Jiangsu, China
[3]Department of Cardiovascular Surgery, Peking University International Hospital, Beijing, China
[4]Institute of 3D Printing, Beijing City University, Beijing, China

Background

Williams syndrome (WS), also known as Williams–Beuren syndrome, is a congenital multisystem disorder that affects the cardiovascular, connective tissue, and central nervous systems [1]. Cardiovascular defects are the primary cause of mortality in patients with WS [2]. Common cardiovascular malformations in WS include supravalvular aortic stenosis (SVAS), peripheral pulmonary arterial stenosis (PPS), coronary artery abnormalities, and other systemic arterial stenoses [3]. The choice of surgical approach is typically guided by the anatomical characteristics of the stenosis [4]. The most common surgical intervention for WS is the augmentation of SVAS [5], which can be performed using several established techniques, including the McGoon, Doty, Brom, and Myers' repair methods [6]. Conventional methods for diagnosing and planning surgeries rely heavily on the physician's expertise and spatial reasoning. However, these traditional approaches often lack visualization tools, quantifiable metrics, and the ability to accurately predict surgical outcomes. This limitation can occasionally result in unfavorable outcomes, such as severe coronary insufficiency postoperatively following the relief of distal aortic obstruction. While hemodynamic changes, such as coronary insufficiency, can be inferred from alterations in vascular morphology, accurately quantifying these changes remains challenging. This limitation affects both surgical decision-making and long-term prognosis. Virtual surgery combined with computational fluid dynamics (CFD) provides a valuable tool for visualizing surgical planning, quantifying hemodynamic parameters, and predicting postoperative hemodynamics. It has become an essential method for improving the understanding of blood flow dynamics in both healthy and diseased vessels. Yu Hohri [7] employed virtual surgery based on CFD to predict postoperative hemodynamics in a patient with restenosis in the ascending aorta (AAo), bilateral coronary arterial aneurysms, and a significantly thickened left ventricular wall. They compared the left coronary flow supply of root replacement within situ Carrel patch coronary reconstruction and coronary artery graft bypass. Similarly, Jie Hu compared the surgical effects on the hemodynamic parameters of McGoon, Doty, and Brom procedures for SVAS based on a 3D model of the aorta and its main branches [8]. Ingrid S. Lan accurately predicted postinterventional pulmonary artery pressures of transcatheter interventions in patients with pulmonary artery stenosis in WS using CFD [9]. Gal et al. developed mean gradient prediction models, comparing Doppler-derived and CFD gradients. They proposed that the diameter ratio between the sinotubular junction (STJ) and the aortic annulus in patients with SVAS could serve as a reliable indicator of the severity of the defect [10]. Jack, J. T pre- and post-surgical geometries and performed CFD to evaluate the effectiveness of surgical intervention in correcting a severe aortic defect in a patient with WS [11]. In addition, a group of researchers has applied CFD to patient-specific pre-surgical planning, design, and optimization of aortic and pulmonary artery repairs using tissue-engineered materials, as well as conducting animal studies to assess postoperative performance [12–14]. However, previous research has not conducted a comprehensive hemodynamic analysis of systemic arterial stenoses in WS. In this study, we performed a detailed hemodynamic evaluation of cardiovascular abnormalities in WS, focusing on major affected blood vessels, including the aorta, carotid artery, coronary arteries, and pulmonary artery. Virtual surgery and CFD were used for both surgical planning and postoperative assessment.

Materials and methods

Study design and case selection

This study was conducted in accordance with the principles of the Declaration of Helsinki and was approved by the Ethics Committee of Peking University International Hospital (Approval No. IRB2019-062). The aim of the study was to predict the surgical outcomes and assess the effectiveness of the repair surgery through hemodynamic simulations, including preoperative, virtual predictive, and postoperative models. A 9-year-old male patient was included in the study. He was preliminarily diagnosed with congenital heart disease, supra-aortic stenosis, mitral insufficiency, cardiac enlargement and sinus rhythm by ultrasonography. As the patient was under 18, informed consent was obtained from his legal guardian.

In the patient's surgical management, 3D modeling and hemodynamic analysis were employed to guide and evaluate the procedure. The preoperative, predictive, and postoperative models were reconstructed and analyzed by engineers under the guidance of the surgical team. A multidisciplinary consultation group discussed the surgical plan, using hemodynamic simulation as a key reference for decision-making. When designing the graft shape and size, potential anatomical changes during the interval between preoperative data collection and surgery were considered. To ensure consistency with the original data, an additional ultrasound examination was performed one day before the surgery.

Clinical data measurement

Cardiac CT data were used to reconstruct the heart. CT scans were obtained with a 256-layer General Electric Revolution scanner (Revolution CT, GE Healthcare, Waukesha, WI, USA) and saved in Digital Imaging and Communications in Medicine (DICOM) format. Doppler transthoracic echocardiography (TTE) was used to obtain flow data at the inlet of aorta. In this study, ultrasound examinations were performed using the Philips EPIQ7 (Philips, NL) system. The velocity-time plot over a cardiac cycle was digitized and smoothed, the velocity data was multiplied by the inlet area to calculate the volumetric flow rate, and then used for the boundary condition definition.

Virtual model construction, surgical design and grid construction

Virtual models included preoperative diagnostic models, predictive surgical models, postoperative models, and models for CFD. The Mimics Innovation Suite 19.0 (Materialise HQ, Leuven, Belgium) software was used for model processing. Preoperative, predictive, and postoperative models were reconstructed using Rhinoceros 6.0 (Robert McNeel & Associates, USA) software and Zbrush 4R9 (Pixologic, Los Angeles, USA) software. For grid construction, ICEM CFD (Fluent, Inc., Lebanon, NH) was used. Each model was meshed with a tetrahedral/mixed meshing scheme. To reduce computational costs, a hybrid mesh was used, particularly considering the size differences between the aorta and coronary arteries. The aorta and coronary arteries were segmented into two separate components and meshed at different resolutions. Grid independence testing was performed using six different grid sizes to ensure the accuracy and reliability of the results (171,967, 272,914, 359,023, 485,539, 659,628, and 1278,603). The model with 659,628 cells was selected for simulation, as the results indicated that global flow features, such as velocity components, remained stable with further grid refinement. Considering that the predictive and postoperative models in subsequent simulations closely resemble the preoperative model in terms of structural characteristics, the same size ($L_{\text{Wall of Aorta}}$=0.9 mm, $L_{\text{Wall of Coronary Artery}}$ =0.4 mm, $L_{\text{Outlet of Aorta}}$=0.7 mm, and $L_{\text{Outlet of Coronary Artery}}$ =0.2 mm) is applied to grid division. The final grid sizes for the preoperative, predictive, and postoperative models were 659,628, 654,685, and 776,030 cells, respectively.

Boundary conditions and CFD simulations

ANSYS Fluent, using the pressure-based solver, was employed to create and compute the solution. Blood flow in large arteries was modeled as a homogeneous Newtonian fluid, with a density of $\rho = 1056$ kg/m^3 and dynamic viscosity of $\mu = 0.0035$ Pa·s [15]. The finite volume method (FVM) was used for discretizing the computational regions. Spatial discretization was performed using the second-order upwind scheme. Pressure-velocity coupling was handled with the SIMPLE (Semi-Implicit Method for Pressure-Linked Equations) algorithm. Turbulent flow was modeled using the SST k-omega turbulence model. A low turbulence intensity of 1%, no-slip conditions, and the assumption of a rigid arterial wall were applied in this study.

The velocity profile at the aortic inlet, measured by Doppler TEE, was converted into mass flow rates and used as the inlet condition for the CFD models. Zero gradient pressure were set as the outlet. The cardiac cycle was set to 0.8 s based on clinical measurements. Additionally, a sensitivity test was conducted to evaluate the effect of time step size on the unsteady simulation results. Four time-steps—0.001s, 0.004s, 0.008s, and 0.016s—were tested. Results showed that further reduction in time step beyond 0.008s had minimal impact on the velocity and pressure distributions. To optimize computational efficiency, a time step of 0.008 s was selected. Each cardiac cycle consisted of 100 time-steps, with 30 iteration steps set for each time step. The calculation of each step ends when the residual converges to 10^{-5} or complete the iteration of 30 steps first. The simulation was run for five cardiac cycles to eliminate period dependency. Convergence was deemed achieved when flow rate and pressure data exhibited periodic repetition, and data from the final cycle was used for analysis.

Once the flow solution converged for each model, the results were analyzed using CFD-POST (Fluent, Inc., Lebanon, NH). In addition to conventional parameters, several additional calculations were performed. Wall Shear Stress (WSS) represents the instantaneous stress applied at the vessel wall. To derive a meaningful conclusion, the Time Average Wall Shear Stress (TAWSS) over a cardiac cycle was calculated [16, 17].

$$TAWSS = \frac{1}{T}\int \mid \overrightarrow{WSS\,(t)} \mid \, dt \tag{1}$$

To assess the temporal oscillations in the immediate WSS vector over the cardiac cycle, the Oscillatory Shear Index (OSI) [18] was used as follows:

$$OSI = 0.5\left(1 - \frac{\mid \int_0^T \overrightarrow{WSS\,(t)}dt \mid}{\int_0^T \mid \overrightarrow{WSS\,(t)} \mid \, dt}\right) \tag{2}$$

Results

The following results are presented for the preoperative, predictive, and postoperative models.

Preoperative models and CFD analysis

The blood pool model, which includes the left ventricle (LV), right ventricle (RV), left atrium (LA), right atrium (RA), aorta (Ao), pulmonary artery (PA) and other cardiac structures, clearly illustrates the cardiac anatomy and helps clinicians identify and understand the location of lesions (Fig. 1a). It showed that cardiovascular stenosis mainly occurs on the Ao. Specifically, there was

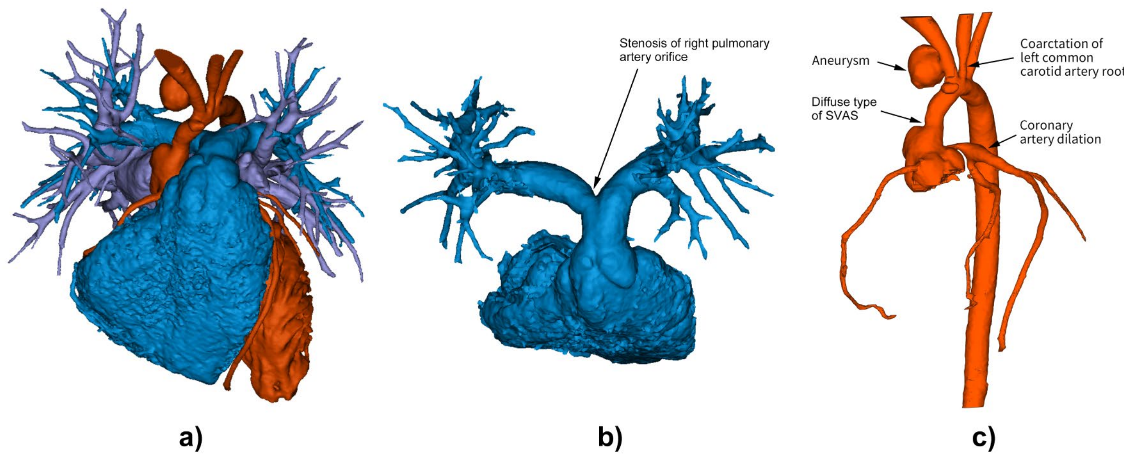

Fig. 1 Preoperative blood pool models. (**a**) Blood pool model including the left ventricle (LV), right ventricle (RV), left atrium (LA), right atrium (RA), aorta, pulmonary artery (PA) and other cardiac structures. (**b**) Venous system model including the pulmonary artery and left ventricle. (**c**) Aorta model showing various lesions

a 5.6 mm stenosis near the right pulmonary artery orifice (Fig. 1b), while no significant stenosis was observed in the left pulmonary artery. The aorta showed SVAS with diffuse, long-segment involvement throughout the entire thoracic aorta, with the narrowest point measuring approximately 6 mm. An aneurysm (28 mm diameter) was identified on the innominate artery, accompanied by severe ostial stenosis of the innominate artery and the left common carotid artery (LCCA). Additionally, the left coronary artery (LCA) exhibited diffuse expansion (Fig. 1c).

In this case, the coarctation of the right pulmonary artery was mild and deemed not requiring surgical intervention. Hemodynamic simulations of the aorta were performed and used for surgical evaluation since the main coarctation or dilation were localized to the aorta.

As shown in Fig. 2a, the velocity streamline distribution illustrates the blood flow in the aorta, with notable acceleration observed at the STJ due to SVAS and coarctation at the root of the LCCA. Distinct eddy currents were observed in the dilated area of the LCA, the innominate aneurysm (IA) and the anterior region of the descending aorta (dAo). In the IA, a slow, circumfluent flow was observed. Blood entered the aneurysm from the upper opening and exited through the lower part of the opening after a rotational flow pattern. Additionally, blood acceleration across the aortic arch (AoA) resulted in complex downstream swirling and recirculation, with a jet impinging on the posterior wall of the dAo. The velocity vector distribution (Fig. 2b) on the cross-sectional view of the aorta illustrates the direction and velocity of the blood flow. The pressure distribution map (Fig. 2c) illustrates the variations in pressure across the blood vessels. Due to the sharp stenosis at the STJ, a significant pressure drop was observed between the upper and lower parts of this region, ranging from 17,000 Pa to 500 Pa ($\Delta P = 123.75$ mmHg). This result is consistent with the pressure drop evaluated via ultrasound, using the Bernoulli equation [19] ($\Delta P = 4\,V^2$), where $V_{max} = 5.6$ m/s, resulting in $\Delta P = 125.44$ mmHg.

Predictive surgical models and CFD analysis

Guided by the preoperative model and hemodynamic analysis, the surgical plan was developed, and a prediction model was established. The primary objectives of the surgery were to widen the SAVS and LCCA stenosis, and to remove the aneurysm on the IA. Additionally, several hemodynamic parameters were considered: expanding the SVAS and LCCA to increase blood flow to downstream vessels, minimizing pressure drops within the vessels, and reducing the values of time-averaged wall shear stress (TAWSS) and oscillatory shear index (OSI). Although the right coronary artery (CA) was dilated, there was no stenosis at the CA orifice. Therefore, no surgical intervention was performed on the coronary arteries due to the patient's young age. A gradually tapered tubular graft was designed from the STJ to the top of the aortic arch (Fig. 3a-c), with a similar approach applied to address the stenosis in the LCCA. The shape and size of the patch were determined based on the difference in diameters between the preoperative and the predictive models (Fig. 3d-e).

Hemodynamic analysis was performed after the virtual aorta model was established. The velocity streamline distribution in the predictive surgical model indicates that blood flow acceleration at the STJ and coarctation at the LCCA root were alleviated, resulting in a more uniform velocity profile along the aorta (Fig. 4a). Aside from minor eddy currents at the LCA expansion and IA, other turbulent flow patterns were eliminated. The maximum

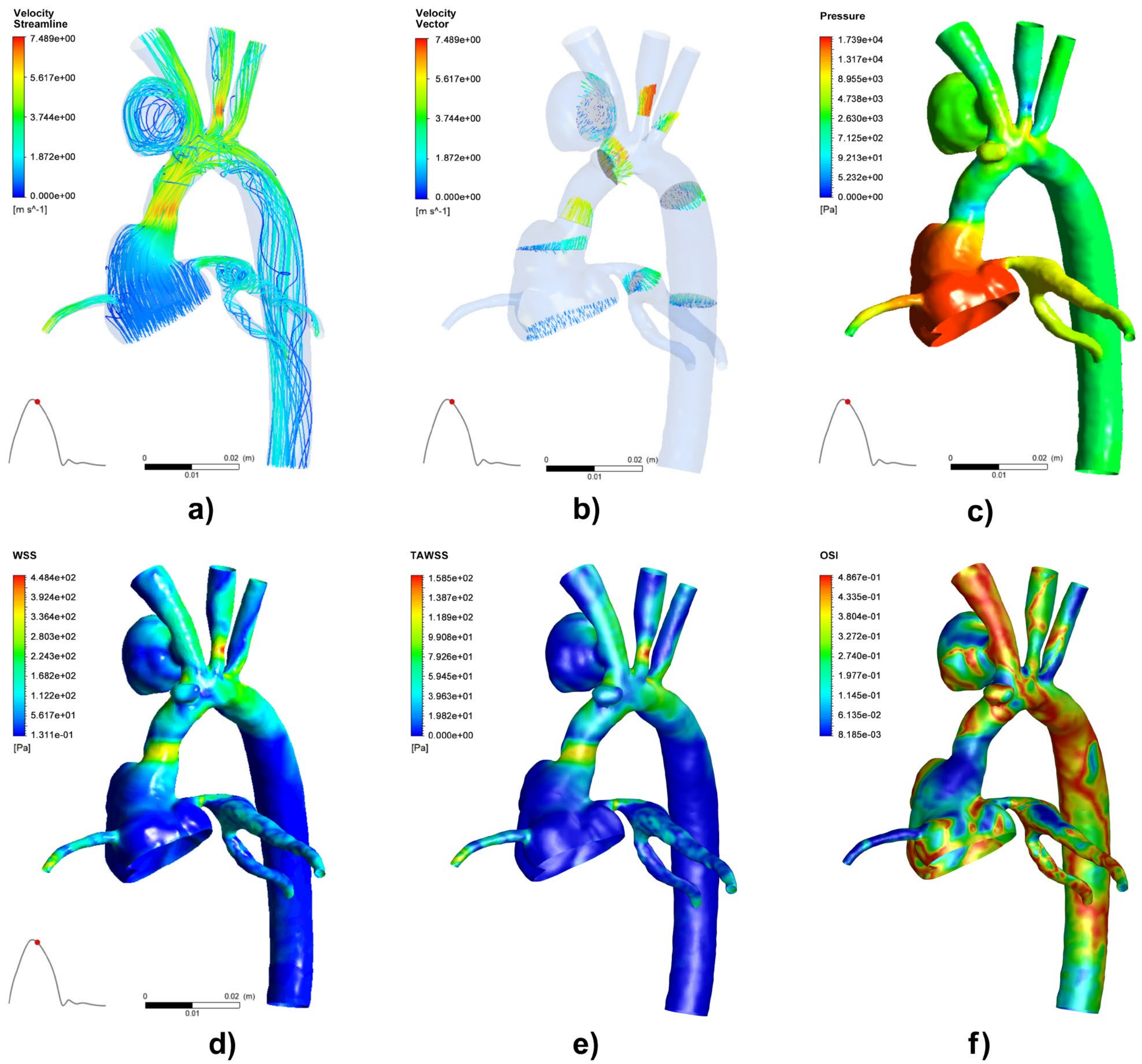

Fig. 2 CFD results of the preoperative model of the Aorta. (**a**) Velocity streamline distribution at the peak of the systolic period. (**b**) Velocity vector on some cross-sections at the peak of the systolic period. (**c**) Pressure distribution at the peak of the systolic period. (**d**) WSS distribution at the peak of the systolic period. (**e**) TAWSS distribution. (**f**) OSI distribution. WSS: wall shear stress; TAWSS: time average wall shear stress; OSI: oscillatory shear index

velocity across all regions decreased from 7.6 m/s to 1.6 m/s. As the severe coarctations were resolved, the pressure on the aortic wall became more stable (Fig. 4b). A uniform WSS distribution was achieved along the entire aorta, with the previously high WSS area between the STJ and the top of the AoA being eliminated (Fig. 4c).

Surgery

After optimization and evaluation, the results of the virtual surgery were used to guide the actual procedure. A polyester artificial blood vessel was cut into a patch based on the calculated shape (Fig. 4f). The tissue at the stenotic region of the Aao and part of the anterior aortic wall of the aortic arch were excised, and the patch was sutured in place to reconstruct the aortic arch. The aneurysm on the innominate artery was removed and the incision was sutured. Additionally, the coarctation at the LCCA was addressed by widening it with a sutured patch.

Postoperative surgical models and CFD analysis

Postoperative CT and ultrasound data were used to reconstruct the aortic model, which was then used to set the inlet flow conditions. The maximum flow rate decreased to 1.5 m/s (Fig. 5a). The maximum pressure on the vessel wall surface was reduced to 1618 Pa (Fig. 5b), and the maximum time-averaged wall shear stress

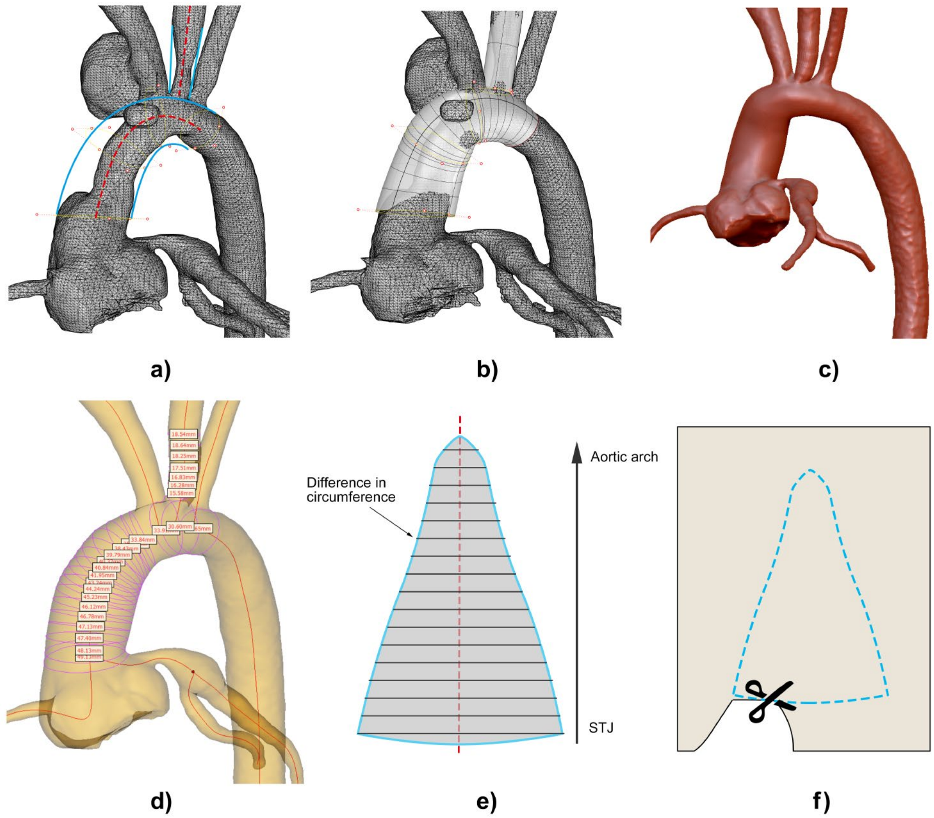

Fig. 3 Design process of virtual surgery. (**a**) Virtual reconstruction of the aortic arch morphology was performed using Rhinoceros 6.0, where point curves were interpolated to define the centerlines and edge lines. The centreline and the edge lines were drawn on both sides of the expected model, and circles were drawn perpendicular to it along the centreline. (**b**) A tapered pipe model was created in Rhinoceros 6.0 using the "sweep by one rail" tool, with the centerline of the simulated blood vessel serving as the path and circular cross-sections at both ends. (**c**) The final aortic model was obtained by smoothing and merging the structure in Zbrush 4R9, using grid fusion techniques. (**d**) The circumference of each aortic cross-section was measured in Mimics Innovation Suite 19.0. (**e**) The shape of the patch was calculated according to the difference between the circumference of the aortic cross section of the prediction model and the preoperative model in Rhinoceros 6.0. (**f**) The calculated shape was used as a template for patch cutting

(TAWSS) decreased to 20.9 Pa (Fig. 5c). The results of the postoperative CFD analysis showed good consistency with the predicted CFD analysis, confirming the accuracy of the surgical plan and its effectiveness in improving hemodynamic conditions.

Morphological comparison of preoperative, predictive, and postoperative models

To compare the morphological changes between the preoperative, predictive, and postoperative models, the circumferences at various sections of the aorta were measured and analyzed. The results showed that the circumference at the location of the greatest expansion increased by 25 mm (Fig. 6). The difference in perimeter between the predictive and postoperative models was minimal, with a mean difference of 1.17 ± 0.23 mm, indicating strong consistency between the predicted and actual outcomes.

Comparison of predictive and postoperative models

To assess the accuracy and effectiveness of surgical planning, a detailed comparison was made between the predictive and postoperative models. Morphologically, the differences between the two models were minimal, with a mean circumference difference of 1.17 ± 0.23 mm. This slight variation is inevitable due to the processes of patch creation, trimming, and suturing during the aortic repair. In terms of hemodynamics, the velocity streamline distributions of the predictive and postoperative models were largely consistent, with a reduction in rotational flow observed in the descending aorta in both models. However, the postoperative model exhibited a larger Aao diameter, resulting in higher downstream outlet flow velocities compared to the predictive model. The distribution of TAWSS was also similar in both models, though differences in numerical values were observed at the junction of the brachiocephalic artery and the aortic arch. The OSI distribution showed more pronounced differences in the lower aortic arch and the inner side of the descending aorta. These variations may be attributed

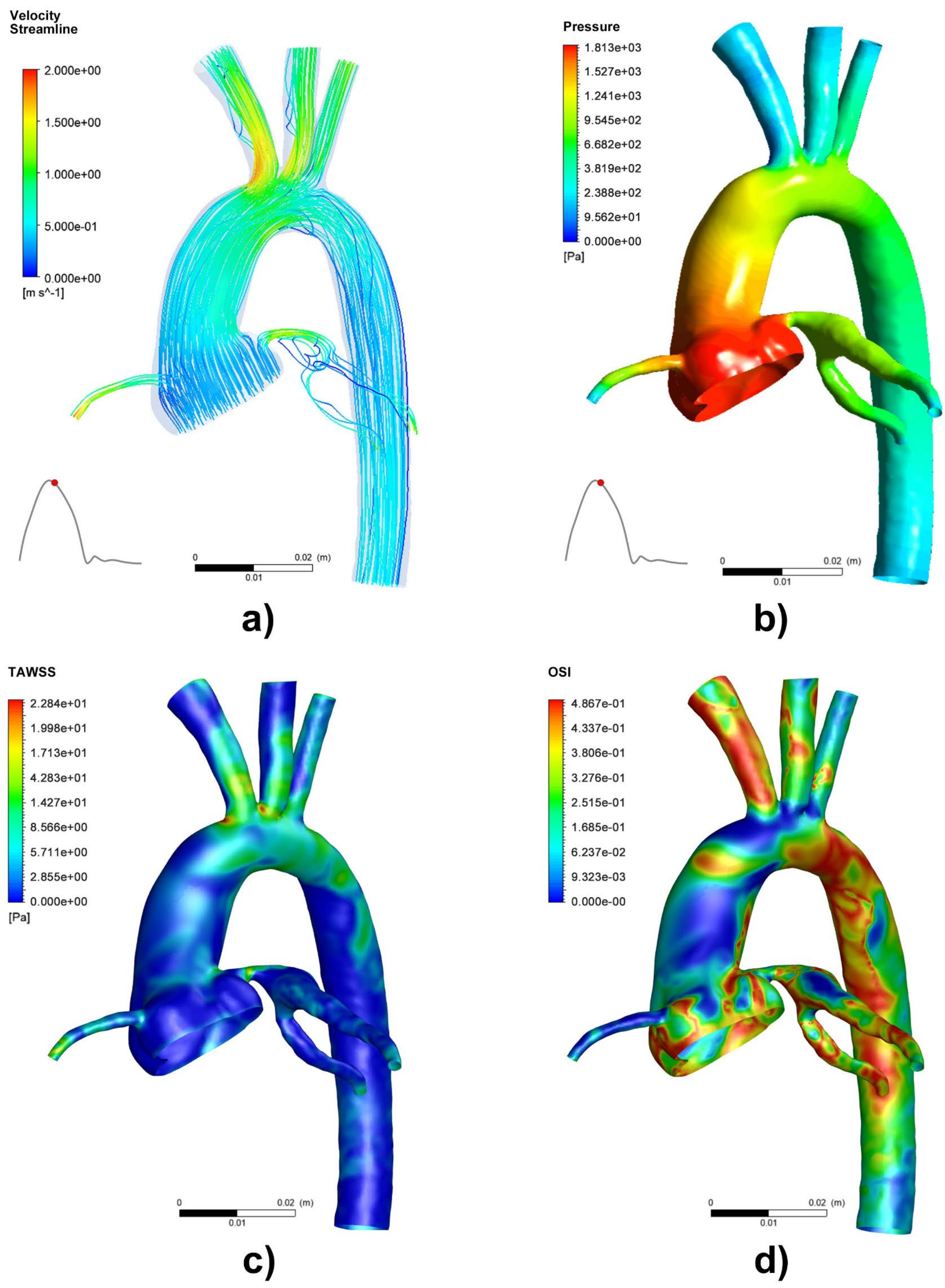

Fig. 4 CFD results of the predictive model of the aorta. (**a**) Velocity streamline distribution at the peak of the systolic period. (**b**) Pressure distribution at the peak of the systolic period. (**c**) TAWSS distribution. (**d**) OSI distribution. TAWSS: time average wall shear stress; OSI: oscillatory shear index

to the differences in size and shape of the aortic arch between the two models. Overall, the predictive and postoperative models demonstrated a high degree of consistency, validating the predictive model as an effective tool for guiding surgical planning.

Discussion

Accurate diagnosis and evaluation of the various cardiovascular abnormalities associated with WS are critical for both surgical management and long-term prognosis. Traditional diagnostic methods and surgical planning

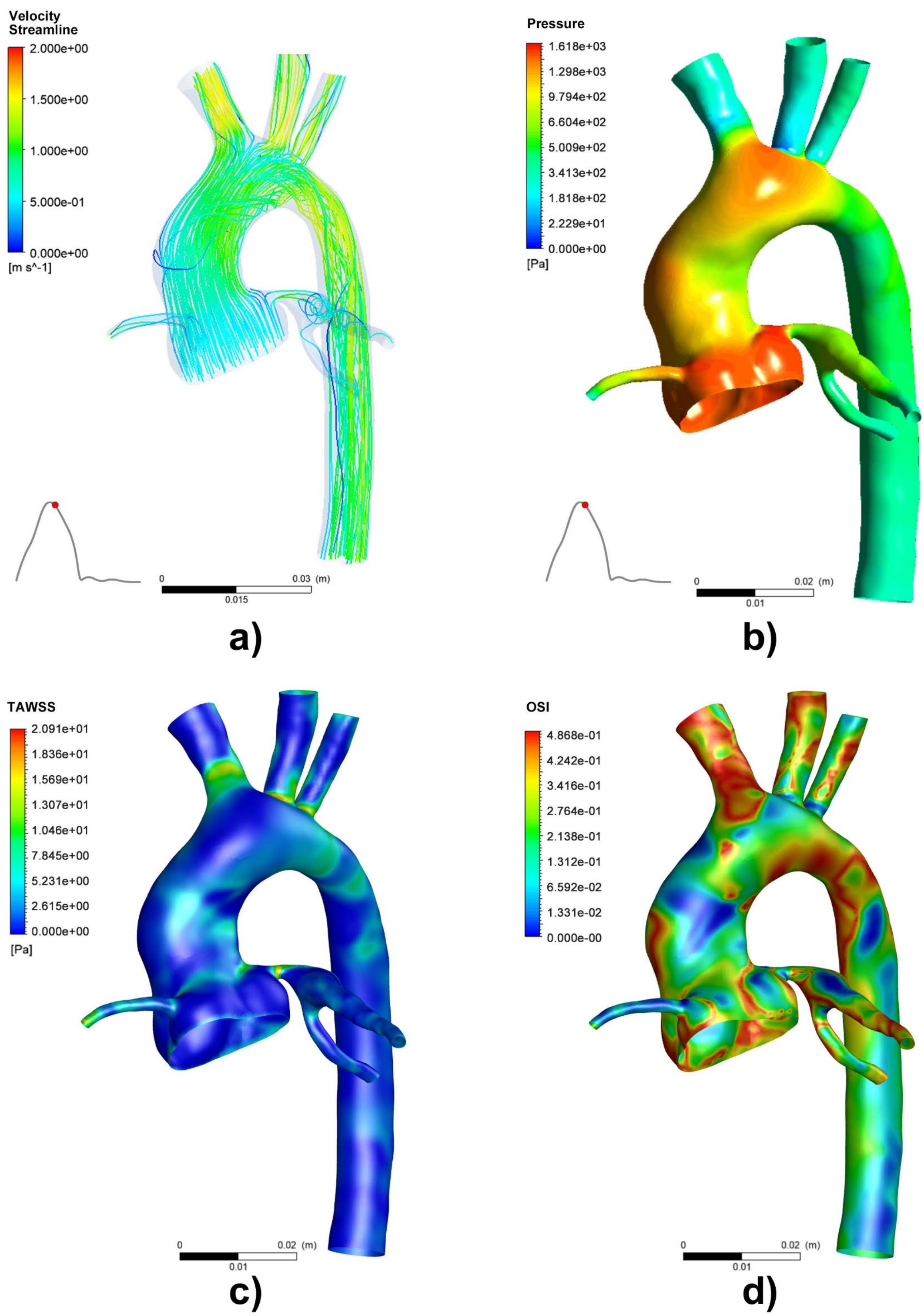

Fig. 5 CFD results of the postoperative model of the aorta. (**a**) Velocity streamline distribution at the peak of the systolic period. (**b**) Pressure distribution at the peak of the systolic period. (**c**) TAWSS distribution. (**d**) OSI distribution. TAWSS: time average wall shear stress; OSI: oscillatory shear index

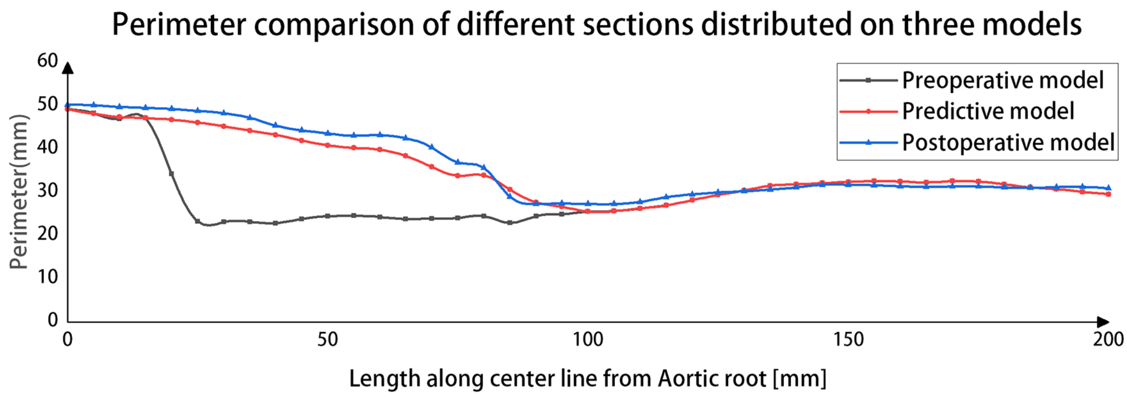

Fig. 6 Perimeter comparison of different sections distributed on three models

often face challenges in predicting postoperative hemodynamic parameters with precision. Virtual models and CFD offer a solution by enabling advanced predictions of surgical outcomes and hemodynamics [20]. The application of hemodynamic analysis and optimization has already been well-established in cardiovascular surgery [12, 21–23]. However, there was no study has performed a comprehensive global hemodynamic analysis of the systemic arterial stenoses in WS. In this study, virtual surgery and CFD were employed for surgical planning, guidance, and postoperative evaluation. Unlike previous studies on CFD in WS [9–12], this research presents the first systematic comparison of postoperative and predictive models. Several critical hemodynamic parameters essential for developing precise surgical strategies were analyzed and compared, providing valuable insights for improving surgical decision-making.

Velocity

The velocity streamline distribution illustrates the impact of stenosis location and severity on blood flow dynamics. In this case, flow acceleration was observed at the STJ, with coarctation at the root of the LCCA. The velocity at the STJ decreased from 5.6 m/s before the operation to 1.6 m/s in the predictive model and 1.5 m/s in the postoperative model. Both the predictive and postoperative models exhibited stable blood flow velocities.

Vortex

Vortex flow was observed in the dilated areas of the LCA, the IA and the anterior region of the dAo. Previous studies suggest that vortical flow structures, with relatively high swirling strength, may contribute to vessel dilation downstream of a coarctation segment [24]. However, in both the virtual and postoperative models, the vortex flow in the IA and dAo regions disappeared, with only the LCA retaining some vortex flow characteristics.

Pressure gradient

The pressure gradient across the coarctation provides valuable insight into the risk of acute complications and the necessity for timely intervention. The pressure is highest at the AAo, and progressively drops at the CoA the supra-aortic branches along the aorta. As the severity of the coarctation decreases, the pressure difference between the ascending and descending aorta gradually diminishes (Figs. 2C, 4B and 5B). With the widening of the STJ, the overall pressure on the whole blood vessel walls decreases. Additionally, computational analysis offers a non-invasive method for estimating the pressure gradient across the CoA [25].

WSS and TAWSS

Accurate estimation of WSS is usually used to predict specific tear locations, whereas abnormal WSS and WSS gradients are often discussed to investigate biological processes that may result in vascular wall remodeling [26]. In the preoperative model, high WSS was observed at the STJ, root of the LCCA and upper part of the AoA. The regional distributions of TAWSS and WSS closely mirrored those of peak systolic WSS, though the values were generally lower during the systolic period. In the prediction model and postoperative model, the area and value of the TAWSS distribution decreased. WSS is determined by many factors, such as blood flow pattern, blood vessel morphology, and blood viscosity [27]. Previous studies have shown that excessively low or high WSS can be associated with risks of atherosclerosis or thrombosis [28]. Abnormally high WSS can alter protein expression on the endothelial cell wall, negatively affecting vessel distensibility and compliance [29]. On the other hand, excessively low WSS (less than 0.5 Pa) can reduce endothelial nitric oxide production, leading to smooth muscle cell proliferation and collagen accumulation [30]. In the preoperative model, high WSS was detected at the STJ, root of the LCCA and upper part of the AoA. The maximum TAWSS value decreased from

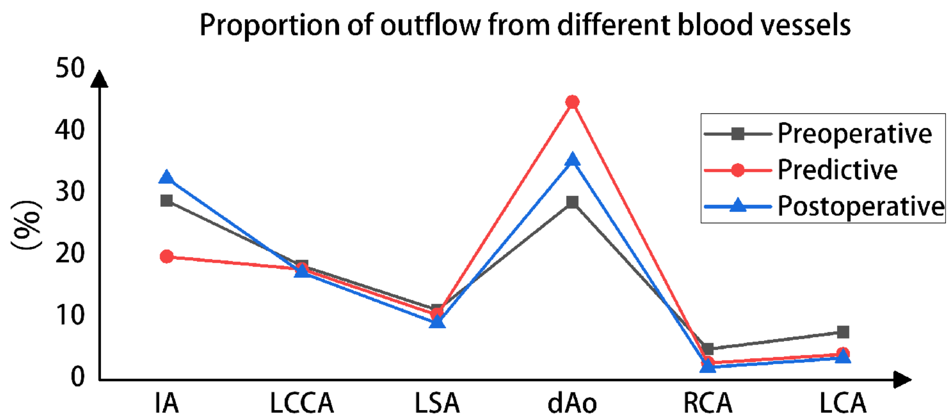

Fig. 7 Proportion of outflow from different blood vessels. IA: innominate artery; LCCA: left common carotid artery; LSA: left subclavian artery; dAo: descending aorta; RCA: right coronary artery; LCA: left coronary artery

158 Pa in the preoperative model to 22.8 Pa in the predictive model and 20.9 Pa in the postoperative model. Overall, the TAWSS values significantly decreased in the postoperative model, aligning with the surgical objectives of reducing hemodynamic stress and promoting better vascular health.

OSI

OSI measures the directional changes in WSS. A low OSI indicates unidirectional WSS, while a value of 0.5 represents bidirectional WSS with a time-averaged value of zero. Previous studies have shown that areas exposed to both high OSI and low TAWSS are at greater risk of rupture, calcification, or wall thickening [31]. In this study, high OSI values were primarily observed in the IA, the lower side of the descending aortic arch, and the downstream vasculature following the expansion of the CA. The OSI values in the downstream regions of these constrictions decreased, reflecting a reduction in flow disruption and potentially lowering the risk of adverse vascular events.

Blood flow ratio

One of the main goals of aortic stenosis dilation surgery is to improve blood flow to downstream vessels. To quantitatively assess the impact of broadening the coarctation of the aorta, the flow through each outlet vessel was monitored and calculated. As shown in Fig. 7, the flow distribution at each outlet exhibited a strong correlation between the predictive and postoperative models. The proportion of outlet flow of dAo (28.7% before the operation) increased both in the prediction CFD (44.9%) and the postoperative CFD (35.5%). In the postoperative CFD, the flow percentage of the IA outlet increased (from 28.94% to 32.59%) reflecting the enlargement of the IA following aneurysm removal and suturing. These changes in flow distribution help explain the dilation of the coronary arteries. Aortic constriction reduces downstream blood flow, which in turn increases the volume of blood directed into the coronary arteries, leading to their dilation. This condition is alleviated after surgery, as the aortic constriction is relieved and normal blood flow is restored.

Hemodynamic analysis based on individual patient data offers valuable insights, enabling doctors to gain a more comprehensive understanding of cardiovascular malformations. Vascular stenosis and other structural lesions in WS can vary in type and location, making it challenging to accurately identify and assess all abnormalities for appropriate surgical planning. Virtual models provide a clear, intuitive representation of the entire cardiovascular structure, helping doctors quickly pinpoint lesion sites. Measurements based on virtual models and CFD analysis can quantify the morphological and hemodynamic characteristics of the whole cardiovascular system, especially the lesion location. This enhances the diagnostic process. In addition, hemodynamic analysis has outstanding advantages in revealing pathogenesis. In this case, CFD effectively highlights key hemodynamic characteristics, providing a solid foundation for guiding surgical decisions.

For the operation of cardiovascular structural diseases, the expected hemodynamic improvement after operation is crucial. However, it is difficult to accurately evaluate the postoperative morphology and hemodynamics through imaging. Similar to diagnosis, whether surgical intervention should be performed, the degree of intervention at different locations, and the expected results are uncertain due to the complexity of WS. The diagnosis and surgical planning mainly depend on the experience of surgeons. The patch is generally made by the surgeon at the operating table in combination with intraoperative exploration and experience, which may prolong the operation time and increase the operation risk.

Virtual surgery and hemodynamic simulation can predict surgical outcomes, enabling doctors to optimize and rehearse procedures in advance. Patches with complex shapes can be calculated before surgery. Additionally, virtual models and 3D-printed blood vessels offer the opportunity for repeated in vitro simulations. These predictable results and preoperative drills are of great significance for reducing intraoperative exploration, shortening the operation time and enhancing the confidence of surgeons.

In this study, the morphological and hemodynamic characteristics of the preoperative, predictive, and postoperative models were analyzed and compared. This comparison confirmed the consistency between the postoperative and predictive models, demonstrating the feasibility of the virtual surgery approach. Additionally, postoperative CFD simulations provided valuable metrics for experts to assess the surgical outcomes and guide future treatment strategies. As hemodynamic analysis can validate the surgical intervention, it also offers further diagnostic insights for the ongoing management of the patient.

This study has several limitations that should be acknowledged. First, only a single case was analyzed, which allowed us to explore the feasibility of the proposed method but did not evaluate its effectiveness across multiple cases. Further studies with larger sample sizes are required to validate these findings. Second, a zero-pressure outlet condition was used instead of dynamic pressure prediction via the 3-element Windkessel method [32]. Because of the use of a zero-pressure outlet, the pressure distributed throughout the entire aorta will decrease compared to the actual value. Lastly, the influence of the aortic valve's opening and closing during the cardiac cycle on hemodynamics was not incorporated into the analysis, which may affect the accuracy of the results.

Conclusions

Hemodynamics based on patient specific virtual models offer intuitive insights that enable doctors to better understand and address cardiovascular malformations. Virtual surgery and CFD can predict the surgical results and allow doctors to optimize and practice the surgery and then guide the cutting of the patch before the operation. The method of predicting surgery through virtual surgery and CFD is accurate and feasible, and it has potential advantages in postoperative diagnosis and follow-up treatment.

Abbreviations

3D	Three-dimensional
AAo	Ascending aorta
Ao	Aorta
AoA	Aortic arch
CA	Coronary artery
CFD	Computational fluid dynamics
CT	Computed Tomography
dAo	Descending aorta
DICOM	Digital Imaging and Communications in Medicine
FVM	Finite volume method
IA	Innominate aneurysm
LA	Left atrium
LCA	Left coronary artery
LCCA	Left common carotid artery
LV	Left ventricle
OSI	Oscillatory shear index
PA	Pulmonary artery
PPS	Peripheral pulmonary arterial stenosis
RA	Right atrium
RPA	Right pulmonary artery
RV	Right ventricle
SIMPLE	Semi-Implicit Method for Pressure Linked Equations
STJ	Sinotubular junction
SVAS	Supravalvular aortic stenosis
TAWSS	Time average wall shear stress
TTE	Transthoracic echocardiography
WS	Williams syndrome
WSS	Wall Shear Stress

Acknowledgements
Not applicable.

Author contributions
Jixiang Liang, Xuewei Fang and Bingheng Lu designed the study. Guangyu Pan and Dianyuan Li provided case information and performed the surgery. Jixiang Liang and Xuewei Fang operated the software for 3D modeling, CFD. Jixiang Liang and Gen Zhang prepared the figures and wrote the main manuscript text. All authors reviewed the manuscript.

Funding
The project was supported by Nanjing Medical University Affiliated Suzhou Hospital Research Grant GSRCKY20210101. The funders had no role in study design, data collection and analysis, decision to publish, or manuscript preparation.

Data availability
The data that support the findings of this study are available from Peking University International Hospital but restrictions apply to the availability of these data, which were used under license for the current study, and so are not publicly available. Data are however available from the authors upon reasonable request and with permission of Peking University International Hospital.

Declarations

Competing interests
The authors declare that they have no competing interests.

Received: 21 September 2024 / Accepted: 25 December 2024
Published online: 04 March 2025

References

1. Kaplan P, Wang P, Francke U. Williams (Williams Beuren) syndrome: a distinct neurobehavioral disorder. J Child Neurol. 2001;16(3):177–90. https://doi.org/10.2310/7010.2001.18071.
2. Game X, Panicker J, Fowler C. Williams-Beuren syndrome. N Engl J Med. 2010;362(3):239–52.
3. Collins RTI. (2018). Cardiovascular disease in Williams syndrome. Current Opinion in Pediatrics 30(5):609 – 15. https://doi.org/10.1097/mop.0000000000000664.
4. Ma M, Martin E, Algaze C, Collins RT, McElhinney D, Mainwaring R, Hanley F. Williams Syndrome: Supravalvar Aortic, Aortic Arch, coronary and pulmonary arteries: is Comprehensive Repair Advisable and Achievable? Seminars

in thoracic and Cardiovascular surgery. Pediatr Cardiac Surg Annual. 2023;26:2–8.
5. Collins RT, Kaplan P, Somes GW, Rome JJ. Long-term outcomes of patients with Cardiovascular abnormalities and Williams Syndrome. Am J Cardiol. 2010;105(6):874–8. https://doi.org/10.1016/j.amjcard.2009.10.069.
6. Wu F-Y, Mondal A, Del Nido PJ, Gauvreau K, Emani SM, Baird CW, Kaza AK. Long-term surgical prognosis of primary supravalvular aortic stenosis repair. Ann Thorac Surg. 2019;108(4):1202–9.
7. Hohri Y, Itatani K, Yamazaki S, Yaku H. Computerized virtual surgery based on computational fluid dynamics simulation for planning coronary revascularization with aortic root replacement in adult congenital heart disease: a case report. Gen Thorac Cardiovasc Surg. 2021;4:69.
8. Hu J, Liu JL, Jiang Q, Zhu YF, Zhang W, Dong W, Zhang HB. (2021). Influence of Surgical Methods on Hemodynamics in Supravalvular Aortic Stenosis: A Computational Hemodynamic Analysis. Pediatric Cardiology 42(8):1730 – 9. https://doi.org/10.1007/s00246-021-02657-3.
9. Lan IS, Yang W, Feinstein JA, Kreutzer J, Collins RT, Ma M, Adamson GT, Marsden AL. (2022). Virtual Transcatheter Interventions for Peripheral Pulmonary Artery Stenosis in Williams and Alagille Syndromes. JOURNAL OF THE AMERICAN HEART ASSOCIATION 11(6) https://doi.org/10.1161/JAHA.121.023532.
10. Gal DB, Lechich KM, Jensen HK, Millett PC, Bolin E, Daily J, Jack JT, Stephens S, Jensen MO, Collins RT. (2022). The Sinotubular Junction-to-aortic annulus ratio as a determinant of Supravalvar aortic stenosis severity. Am J Cardiol 164(118 – 22.
11. Jack JT, Jensen M, Collins RT, Chan FP, Millett PC. Numerical study of hemodynamic flow in the aortic vessel of Williams syndrome patient with congenital heart disease. J Biomech. 2024;168:112124.
12. Aslan S, Loke YH, Mass P, Nelson K, Yeung E, Johnson J, Opfermann J, Matsushita H, Inoue T, Halperin H, Olivieri L, Hibino N, Krieger A. (2019). Design and Simulation of Patient-Specific Tissue-Engineered Bifurcated Right Ventricle-Pulmonary Artery Grafts using Computational Fluid Dynamics. 2019 IEEE 19th International Conference on Bioinformatics and Bioengineering (BIBE):1012 – 8. https://doi.org/10.1109/BIBE.2019.00188.
13. Aslan S, Liu X, Wu Q, Mass P, Loke Y-H, Johnson J, Huddle J, Olivieri L, Hibino N, Krieger A. Virtual planning and patient-specific Graft Design for aortic repairs. Cardiovasc Eng Technol. 2024;15(2):123–36. https://doi.org/10.1007/s13239-023-00701-2.
14. Hayashi H, Contento J, Matsushita H, Mass P, Cleveland V, Aslan S, Dave A, Santos Rd, Zhu A, Reid E, Watanabe T, Lee N, Dunn T, Siddiqi U, Nurminsky K, Nguyen V, Kawaji K, Huddle J, Pocivavsek L, Johnson J, Fuge M, Loke Y-H, Krieger A, Olivieri L, Hibino N. Patient-specific tissue engineered vascular graft for aortic arch reconstruction. JTCVS Open. 2024. https://doi.org/10.1016/j.xjon.2024.02.012. 18(209 – 20.
15. Jung J, Hassanein A. Three-phase CFD analytical modeling of blood flow. Med Eng Phys. 2008;30(91–103). https://doi.org/10.1016/j.medengphy.2006.12.004.
16. Banks J, Bressloff NW. Turbulence modeling in three-dimensional stenosed arterial bifurcations. Journal of Biomechanical Engineering; 2006.
17. Qingzhuo C, Huimin C, Mu L, He Y, Luan Y. Haemodynamic analysis of the relationship between the morphological alterations of the Ascending Aorta and the type a aortic-dissection disease. Fluid Dynamics Mater Process. 2021;17(4):721–43.
18. He XJ, Ku DN. (1996). Pulsatile flow in the human left coronary artery bifurcation: Average conditions. Journal of Biomechanical Engineering-Transactions of the Asme 118(1):74-82. https://doi.org/10.1115/1.2795948.
19. Harris P, Kuppurao L. Quantitative doppler echocardiography. Bja Educ. 2016;16(2):46–52.
20. Cherry MA. (2022). Efficient cardio-vascular 4D-flow MRI enabled CFD to improve in-silico predictions of post-surgical haemodynamics in individual patients.
21. Silva-Jr JM, Menezes PFL, Lobo SM, de Carvalho FHS, de Oliveira MAN, Cardoso Filho FNF, Fernando BN, Carmona MJC, Teich VD, Malbouisson LMS. Impact of perioperative hemodynamic optimization therapies in surgical patients: economic study and meta-analysis. BMC Anesthesiol. 2020;20:1–12.
22. Gundert TJ, Marsden AL, Yang W, LaDisa JF Jr. (2012). Optimization of cardiovascular stent design using computational fluid dynamics.
23. Liu X, Aslan S, Hess R, Mass P, Olivieri L, Loke Y-H, Hibino N, Fuge M, Krieger A. (2020). Automatic shape optimization of patient-specific tissue engineered vascular grafts for aortic coarctation. 2020 42nd Annual International Conference of the IEEE Engineering in Medicine & Biology Society (EMBC):2319-23.
24. Zhang X, Luo M, Fang K, Li J, Peng Y, Zheng L, Shu C. (2020). Analysis of the formation mechanism and occurrence possibility of Post-Stenotic Dilatation of the aorta by CFD approach. Computer Methods and Programs in Biomedicine 194(105522.
25. Rinaudo A, D'Ancona G, Baglini R, Amaducci A, Follis F, Pilato M, Pasta S. Computational fluid dynamics simulation to evaluate aortic coarctation gradient with contrast-enhanced CT. Comput Methods Biomech BioMed Eng. 2015;18(10):1066–71.
26. Meng H, Tutino V, Xiang J, Siddiqui A. High WSS or low WSS? Complex interactions of hemodynamics with intracranial aneurysm initiation, growth, and rupture: toward a unifying hypothesis. Am J Neuroradiol. 2014;35(7):1254–62.
27. Resnick N, Yahav H, Shay-Salit A, Shushy M, Schubert S, Zilberman LCM, Wofovitz E. (2003). Fluid shear stress and the vascular endothelium: for better and for worse. Progress in Biophysics & Molecular Biology 81(3):177 – 99. https://doi.org/10.1016/s0079-6107(02)00052-4.
28. Boumpouli M, Sauvage EL, Capelli C, Schievano S, Kazakidi A. Characterization of flow dynamics in the pulmonary bifurcation of patients with repaired tetralogy of fallot: a computational approach. Front Cardiovasc Med. 2021;8:703717.
29. Davies PF, Barbee KA, Lal R, Robotewskyj A, Griem ML. (1995). Hemodynamics and atherogenesis - endothelial surface dynamics in flow signal-transduction. Atherosclerosis Iii: Recent Advances in Atherosclerosis Research: The Third Saratoga International Conference on Atherosclerosis in Nekoma 748(86–103.
30. Gimbrone MA, Topper JN, Nagel T, Anderson KR, Garcia-Cardena G. (2000). Endothelial dysfunction, hemodynamic forces, and atherogenesis. Atherosclerosis V: The Fifth Saratoga Conference 902(230 – 40.
31. Rafiei D, Abazari MA, Soltani M, Alimohammadi M. The effect of coarctation degrees on wall shear stress indices. Sci Rep. 2021;11(1):12757.
32. Antonuccio MN, Mariotti A, Fanni BM, Capellini K, Capelli C, Sauvage E, Celi S. Effects of uncertainty of outlet boundary conditions in a patient-specific case of aortic coarctation. Ann Biomed Eng. 2021;49(12):3494–507.

Publisher's note